CrossMark

Graphitic Carbon Nitride with S and Fe(III) Codoping for Improved Photodegradation Performance
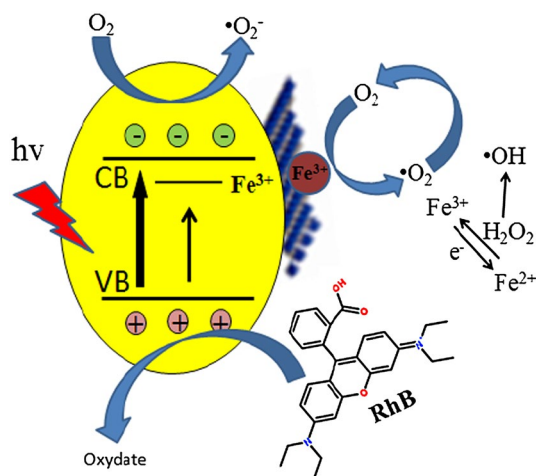
Hailong Dou[1] · Shaohui Zheng[1] · Yongping Zhang[1]

Abstract
The visible light photocatalytic performance of graphitic carbon nitride (g-C_3N_4) can be enhanced by tuning its electronic structure and bandgap via metal and nonmetal elements doping. The Fe and S codoped g-C_3N_4 is synthesized by the polymerization of melamine, iron chloride and trithiocyanuric acid at elevated temperature and characterized as crimped nanosheets with mesoporous structures. The photocatalytic performance of Fe–S codoped g-C_3N_4 for RhB degradation increases seven times by enhancing visible light adsorption and increasing the mobility of photoinduced electron/hole pair by narrowing its bandgap compared to the pure g-C_3N_4 nanosheets. The synergetic effect of Fe(III) ion coordinated in the pore centre among three triazine units and S dopant substituted the N in triazine skeleton causes much stronger delocalized HOMO and LUMO and increases the reactive sites, facilitating the migration of photogenerated charge carriers, thus enhances the visible-light driven photocatalytic performance.

Graphical Abstract

1 Introduction

Resource deficiency, energy shortage and environmental deterioration have become the grand challenges human society has ever faced, it is thus considered as one of the prospective strategy to develop novel materials that can utilize the solar resources effectively and efficiently through technology

✉ Yongping Zhang
  zhangyyping@yahoo.com

[1] Faculty of Materials and Energy, Southwest University, Chongqing 400715, China

innovation. Photocatalysts provided certain promising approaches in water splitting for H_2 evolution and pollutant degradation using solar energy directly and aroused considerable interests for research experts in materials science and chemistry. It is the band structure of semiconductor based photocatalysts that influences the generation, recombination, and transfer of photoinduced electron/hole pairs. Scientists have paid overwhelming attentions to design materials with suitable bandgap and to tune their bandgap to enhance the photocatalytic performance. The graphitic carbon nitride (g-C_3N_4) has layered structure similar to graphene and possesses an appropriate band structure and bandgap of 2.7 eV allowing it to serve as a visible light driven photocatalyst for solar resource conversion [1–3]. Besides its advantages of high stability, low-cost precursors and nonmetal photocatalyst, application was restricted by its intrinsic shortcomings, such as small specific surface area and rapid recombination of the photogenerated electron–hole pairs.

Great endeavors have been made to improve its performance ever since its emergence as a photocatalyst. One category of strategies have been adopted to improve the photocatalytic performance of g-C_3N_4 by the means of the fabrication of nano/mesoporous structures with a soft or hard template [4–6], to increase the specific surface area, thus improve photon absorption in the visible light region. Another strategies try to engineering the band structures of catalysts to separate the electron/hole pair effectively by forming heterojunction with other semiconductors [7, 8], coupling with metal particles [9–13], and doping metal or non-metal elements [14–26], etc. Taken its unique atomic structure into consideration, transition metal elements coordinated in the pore centre among three tri-s-triazine units showed great possibility to enhance the visible light photocatalysis of g-C_3N_4, by forming discrete doping energy level slightly below conduction band. Research results showed that the electrons can be excited from valence band to Fe^{3+}/Fe^{2+} doping energy for Fe doped g-C_3N_4, serving as an acceptor of the photoinduced electrons; photoinduced charge can transport from conduction band to the doping energy level, thus the photoinduced charge can be separated easily [22–25]. Nonmetal doping can tune the electronic structure by forming localized energy states and facilitating the transfer of photogenerated charge carriers. The g-C_3N_4 structure features the pores among three tri-s-triazine units by calcining the cyanic species (e.g. melamine, cyanamide, and dicyandiamide), and the pores are surrounded with nonbonding sp^2 orbitals of nitrogen atoms in the sp^2-hybridazed C–N networks. Thus the pores provide ideal position for the coordination of transition metal ions, and the metal ions coordinated in g-C_3N_4 may modify the electronic structure. Some experimental and theoretical results reported the metal (Fe, Cu) [22–26] and nonmetal (B, O, P, S) [14–21] doping for improved photocatalytic performance. Our previous

work reported that the bandgap was modified by S and O doping [18]. Some experimental results were reported that the Fe doped g-C_3N_4 can improve its photocatalytic performance to certain degree. Fundamental understanding the separation and transformer of photoinduced electron and hole and understanding the photocatalytic reaction pathway are needed since many aspects in this complex process are devoid of direct evidence. Therefore, further experimental and theoretical investigations are needed to gain deeper insight into the mechanism of photocatalytic performance via metal and nonmetal element doping.

In this paper, we reported a pathway to improve the photocatalytic performance by introducing Fe and S atoms into g-C_3N_4 lattice. The experiments revealed that the Fe-S codoped g-C_3N_4 exhibits superior photodegradation for RhB under visible light irradiation. Density functional theory (DFT) showed that the Fe and S doping decreases the bandgap and increases the reactive sites, facilitating the transfer of photogenerated electron–hole pairs.

2 Experimental Details

2.1 Synthesis of the Pure, Fe doped, Fe–S Codoped g-C_3N_4

The pure g-C_3N_4 (CN) was prepared by thermally heating melamine (M) powder (3.78 g) at 550 °C for 2 h under nitrogen atmosphere. Iron chloride ($FeCl_3$, 0.0161 g) was dissolved into 60 mL deionized water, and 10 mL nitric acid (65% concentration) was added. Then the solution was fully mixed with 3.78 g melamine (dissolved in 30 mL methanol) inside a beaker and dried at 60 °C overnight. The obtained white substance of 2.52 g was mixed with 1.71 g trithiocyanuric acid (TCA), and ground into powder and then transferred to a silica boat with a cover and heated at 550 °C for 2 h under nitrogen environment. The obtained Fe–S codoped g-C_3N_4 (Fe–SN) product was yellow powder and collected for further use. The Fe doped g-C_3N_4 (Fe–CN) was prepared in the same way without TCA involved in the preparation process.

2.2 Characterization

The morphology was observed by a scanning electron microscope (SEM, JSE-7800F, Jeol). The X-ray diffraction (XRD) patterns were performed to characterized the crystalline structures of the g-C_3N_4 by a Shimadzu XRD 7000 instrument with Cu Kα radiation ($\lambda = 1.5418$ Å). Fourier transform infrared (FTIR) was measured using a Perkin Elmer spectroscopy instrument in KBr pellets. X-ray photoelectron spectroscopy (XPS) was carried out to analyze the chemical state and composition on a VG ESCALAB

250 spectrometer with Al Kα radiation (hν = 1486.8 eV). Ultraviolet–Visible (UV–Vis) absorption spectra were performed on U-3310 spectrophotometer (Hitachi, Japan) in the wavelength range of 300–800 nm. Photoluminescence (PL) spectra were carried out on a F-7000 fluorescence spectrophotometer (Hitachi, Japan) with an excitation wavelength at 273 nm using a 150 W Xe lamp as the excitation source. The Brunauer–Emmett–Teller (BET) surface area was tested with an ASAP-2010 analyzer. The photocurrent measurements were obtained by a electrochemical workstation in a standard three-electrode system, using a platinum wire and the saturated Ag/AgCl electrode as the counter electrode and reference electrode, respectively. The working electrode was prepared by coating the catalysts on a 1.8 cm × 1.2 cm fluorine-doped tin oxide (FTO) glass substrate. A 300 W Xe lamp with a 420 nm cut-off filter was used as a light source.

2.3 Photocatalytic Performance

The photocatalytic performance was examined by monitoring the degradation of Rhodamin B (RhB) in an aqueous solution under visible light irradiation using a 300 W Xe lamp as light source. 30 mg of photocatalyst was dispersed in RhB aqueous solution (60 mL, 12 mg/L). Prior to irradiation, the suspension was magnetically stirred in the dark room for 30 min to reach sorption equilibrium. During the photocatalysis process, 1 mL of the sample was withdrawn from the reaction cell at 10 min intervals for the measuring the characteristic UV–Vis absorption spectra after centrifugation. The maximum absorption peak was recorded for evaluating the concentration of RhB. The degradation rate of RhB can be calculated by definition:

$$\text{Degradation rate} = \frac{(C_0 - C_t)}{C_0}$$

where C_0 is the sorption equilibrium concentration of RhB and C_t is the concentration of RhB at reaction time t.

3 Results and Discussion

The pure g-C_3N_4 appeared as a blocky structure with some crinkled flakes, as shown in Fig. 1a. The Fe doped g-C_3N_4 in Fig. 1b appeared as the lamellar structure and crimped g-C_3N_4 sheets. The Fe and S codoped g-C_3N_4 sheets in Fig. 1c became the lamella structures curved even more than that of the Fe doped g-C_3N_4 with more irregular porous structures. The mesoporous structures may be resulted by the decomposition of TCA during polymerization process, while the crimped structures are arisen from the larger radii of doped Fe and S element than the host C and N atoms [23]. The Fe + S codoped g-C_3N_4 has a large number of

mesopores, which demonstrate a higher specific surface area, and easy transportation of pollutant to interior surface via the interconnected mesopores. The energy dispersive X-ray spectrum (EDS) analysis showed that composition of the Fe–S codoped g-C_3N_4 comprising rich carbon (C) and nitrogen (N) with dispersed Fe and S elements. The overlapped C, N, Fe and S element EDS image (Fig. 1d) showed the Fe and S elements are dispersed in g-C_3N_4 sheets. The EDS elemental mappings in Fig. 1e–h indicated clearly that the Fe and S elements are distributed discretely on the continuous C, N elemental background.

The Fe and S codoped g-C_3N_4 exhibited the maximum specific surface area among these three samples, as in the nitrogen adsorption–desorption isotherm showed in Fig. 1i. The specific surface area is 13.402, 35.014, and 42.265 m^2/g for the pure, Fe, and Fe + S doped g-C_3N_4 catalysts, respectively. Figure 1i indicated that the apparent curves follow the Type IV adsorption–desorption isotherm with H$_3$ hysteresis loop, which is mainly arisen from the massive presence of mesopores. Therefore, Fe + S codoped photocatalyst will provide more active sites, facilitating photocatalytic activity.

The crystal structure of the pure g-C_3N_4 nanosheets, the Fe-doped and the Fe–S codoped g-C_3N_4 was demonstrated by their XRD patterns. Figure 2a showed the XRD pattern for the pure g-C_3N_4 displays two distinct diffraction peaks located at 2θ of about 13.1° and 27.3°, which are in good accordance with the characteristic peaks of g-C_3N_4. The peak for (100) plane corresponds to the repeating tri-s-triazine unit with a period of 0.67 nm, which is slightly smaller than the theoretical value of 0.73 nm. That demonstrated that the structure of g-C_3N_4 layer corrugated slightly after polymerization of melamine. The peak for (002) crystal plane of g-C_3N_4 is attributed to the lattice planes of the stacking of the conjugated aromatic systems in layered structure with the distance of 0.33 nm [15, 18]. This illustrated the g-C_3N_4 has layered structure similar to graphite. With Fe doped g-C_3N_4, the 2θ position for lattice peak (002) increase a little bit to 27.5° from 27.3° of the pure g-C_3N_4. This indicated that the interplanar stacking distance becomes smaller after Fe doping, since the dopant of Fe(III) ion increased the atomic interaction of interlayer. The stronger attraction between the g-C_3N_4 layers would result in shorter interplanar distance [23]. While the 2θ position for the (002) peak decreased to 27.1° from 27.3° for the Fe + S codoped g-C_3N_4, since the dopant of S has bigger radius than the N atom in the ring structures. This results in the bigger interplanar distance [18]. The XRD results indicate that the Fe and S atoms have incorporated in the g-C_3N_4 layer, and slightly doping of Fe and S has no significant effect on the crystal structure of g-C_3N_4.

The FTIR spectra of the pure g-C_3N_4 nanosheets, the Fe-doped and the Fe–S codoped g-C_3N_4 were depicted in Fig. 2b, in which the typical characteristic peaks at 1228,

Fig. 1 The SEM images of
a pure g-C$_3$N$_4$ nanosheets, **b**
Fe doped and **c** Fe-S codoped
g-C$_3$N$_4$. EDS elements over-
lapped images of C, N, Fe and
S (**d**) and mappings for C (**e**), N
(**f**), S (**g**) and Fe (**h**). **i** Nitrogen
adsorption–desorption isotherm
of pure and Fe + S doped
g-C$_3$N$_4$
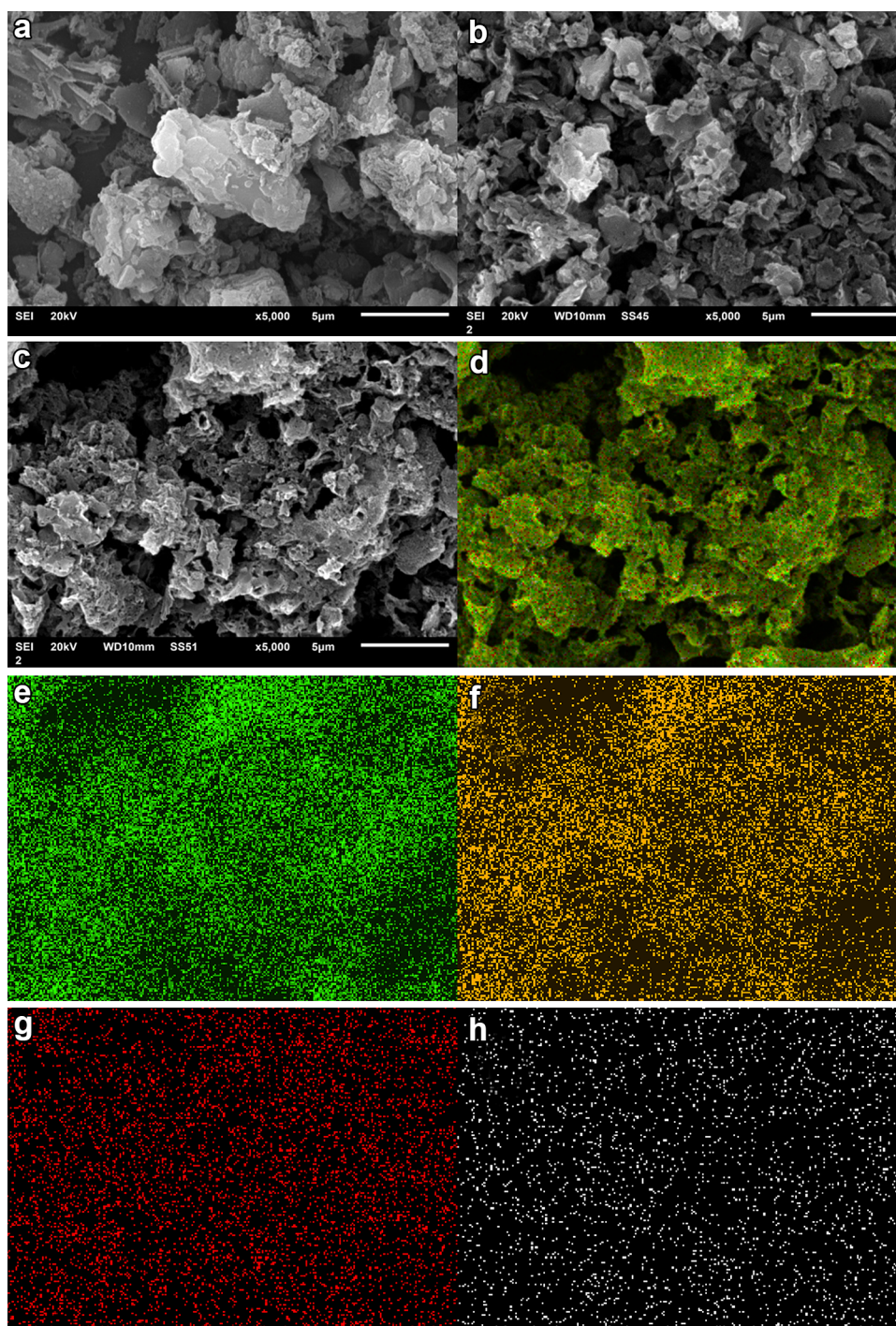
1312, 1390, 1534, and 1625 cm^{-1} can be assigned to the
stretching modes of the aromatic C–N heterocycle and peak
at 805 cm^{-1} is ascribed to the breathing mode of the triazine
units. This demonstrated that g-C$_3$N$_4$ was kept intact struc-
ture of the original graphitic C–N network. The broad peaks
at 3000–3400 cm^{-1} are ascribed to the stretching modes of
N–H, indicating there exist N–H bonds at the edge of the
polymerized triazine. Compared to the pure g-C$_3$N$_4$, a new
peak at 1024 cm^{-1} appears in FTIR spectra for the Fe–S

codoped g-C$_3$N$_4$, which can be attributed to the stretching
mode of C–S bond, which confirms the sulfur are doped into
g-C$_3$N$_4$ lattice [18]. This is consistent with the FTIR results
of the stretching vibration of C–S for the S doped g-C$_3$N$_4$. It
is noteworthy that the FTIR spectrum does not change after
Fe doping, which demonstrates the Fe ion has little interac-
tion with the aromatic C–N rings.

Figure 3 showed the high-resolution XPS spectra of C,
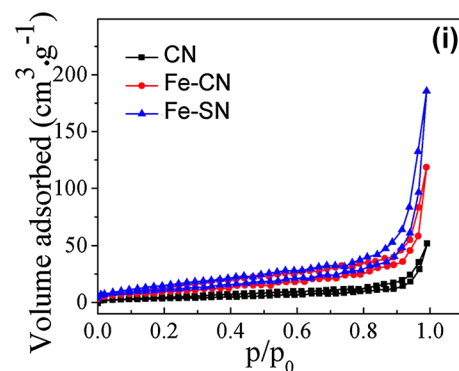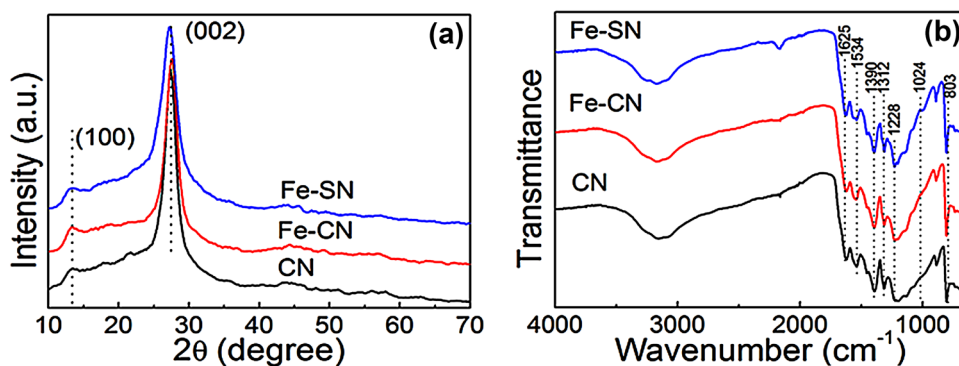N, Fe and S elements the pure g-C$_3$N$_4$, and the Fe-doped,

Fig. 1 (continued)

Fig. 2 XRD patterns (**a**) and FTIF spectra (**b**) of the pure (CN), Fe doped (Fe–CN) and Fe–S codoped (Fe–SN) of g-C_3N_4

Fe–S codoped g-C_3N_4. The high-resolution C 1s XPS spectra of the three samples were shown in Fig. 4a. For the pure g-C_3N_4 nanosheets, the peaks centered at about 288.0 eV (C1) is typically attributed to the sp^2 hybrid C atoms bonded to N-containing aromatic skeleton rings (N–C=N) coordination. The peak at 285.28 eV (C2) is attributed to C–NH_2 bonded in the triazine ring of the reactant intermediary product [10, 18]. The peak at 284.4 eV (C3) could be attributed to the graphite carbon [15]. The N 1s spectra for the pure g-C_3N_4, and the Fe-doped, Fe–S codoped g-C_3N_4 in Fig. 4b can be mainly decomposed to three typical peaks located at about 398.4 eV (N1), 399.7 eV (N2), 400.8 eV (N3), which could be attributed to the sp^2-hybridized aromatic N atoms bonded to carbon atoms (C–N=C), and sp^3-hybridized N atoms of N(–C)$_3$ and terminal amino functions (C–NH_2), respectively [18, 19]. The S atomic dopant do not change the binding energy of C 1s spectrum since the element S has similar electronegativity compared to C atom. For Fe dopant, C 1s and N 1s spectra shifts to higher binding energy. The formation of Fe–N coordinated bond after doping Fe ion in g-C_3N_4 layer, in which Fe provides empty orbit and N provides electron for the Fe–N bond formation. This results in the decrease of electronic density of state (DOS) around the C and N atoms. The binding energy of C 1s and N 1s increases therefore to higher binding energy to balance the binding force for N nucleus for outer electrons.

The Fe 2p spectrum for the Fe-doped, Fe–S codoped g-C_3N_4 in Fig. 4c, the peaks at 710.4 and 723.7 eV are ascribed to the splitting orbits of Fe 2$p_{3/2}$ and 2$p_{1/2}$, which demonstrates that Fe(III) ion to form coordinated bond with the edge N atoms of hepazine. The weak broad peak at 717.5 eV is ascribed to Fe(III) satellite feature similar to that of Fe_2O_3, while the Fe(II) 2$p_{3/2}$ satellite feature of FeO is usually located at 715.0 eV. That demonstrates that Fe atom is imbedded in the pore centre among three tri-s-triazine units of g-C_3N_4 in the oxidation state of Fe(III) ion by forming Fe–N bonds [22–24]. As for the Fe–S codoped g-C_3N_4, a S 2p peak located at 163.1 eV can be reasonably assigned to C–S bonds formed in g-C_3N_4 lattice via substituting N. The peak at 168.3 eV is ascribed to S=O in the intermediate product of sulfoxide resulting from the decomposing TCA [18]. By removing the adventitious carbon contamination, the C/N atomic ratio is 0.76 for the pure g-C_3N_4, which is fairly close to the stoichiometric value of g-C_3N_4. The C/N atomic ratio for the Fe, S codoped g-C_3N_4 is about 0.81, which is slightly larger that that of the pure g-C_3N_4. XPS results show that the Fe and S atoms have been doped into g-C_3N_4 lattice and may preferentially substitute N atoms. For the Fe–S codoped g-C_3N_4, the S content of atomic percentage is about 0.08% and the Fe content is about 0.09%. Taken XPS and XRD results into consideration, Fe ions were suggested to position in the pore centre among
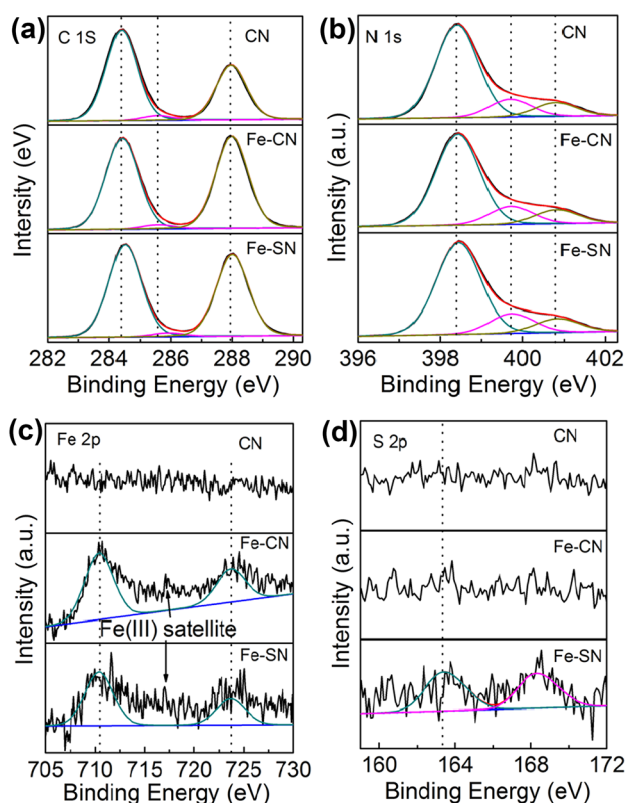
Fig. 3 XPS high resolution spectra for C 1s (**a**) and N 1s (**b**), Fe 2p (**c**) and S 2p (**d**) of the pure g-C$_3$N$_4$ nanosheets (CN) and Fe doped g-C$_3$N$_4$ (Fe–CN) and Fe–S codoped g-C$_3$N$_4$ (Fe–SN)

three tri-s-triazine units by forming Fe–N bonds with the unbonded sp^2 electrons of N atoms.

The UV–Vis diffuses absorbance spectra of the pure, Fe doped and Fe–S codoped g-C$_3$N$_4$ were shown in Fig. 4a. There is a sharp absorption edge for the pure g-C$_3$N$_4$ nanosheets at around 460 nm indexing to the bandgap energy of about 2.7 eV, which is firmly associated with the photo-catalytic property in visible light [18, 19]. It shows enhanced visible light absorption intensity and the red shift edge via Fe and S doping. The Kubelka–Munk plots in Fig. 4b show that the adsorption edge is red shifted with lower bond-ing energy of 2.6 eV for the Fe-doped g-C$_3$N$_4$ and 2.54 eV for the Fe–S codoped g-C$_3$N$_4$. The absorption intensity is remarkably enhanced in the visible region after the Fe and S doping [26]. SEM images have shown that Fe and S doping causes the g-C$_3$N$_4$ sheets curling up. The crimped structure facilitates the n–π* transitions. These results reveal that the Fe–S doping g-C$_3$N$_4$ composites could significantly promote the optical absorption performance and enhance the utilized efficiency of solar light, which subsequently results in its promotion of the photocatalytic activity [25].

The PL spectra were carried out to investigate the recom-bination/separation of photoinduced charge carriers in the pure g-C$_3$N$_4$ nanosheets, the Fe doped and the Fe–S codoped g-C$_3$N$_4$ under the excitation wavelength of 274 nm. The measured PL spectra, as shown in Fig. 4c, showed that all of the samples exhibit a main emission peak appearing at about 440 nm, which is consistent with the reported value in the literatures [16, 17]. Compared to the pure g-C$_3$N$_4$, the Fe doped and the Fe–S doped g-C$_3$N$_4$ show the weaker PL intensity revealing the lower recombination probability of photoinduced electrons and holes [17], which could give rise to a higher photocatalytic activity.

The electrochemical impedance spectra (EIS) of the pure g-C$_3$N$_4$ and the g-C$_3$N$_4$ doped with Fe and S were measured to understand the photocatalytic mechanism. The arc on the EIS Nyquist plot indicates the charge transfer resistance. Generally speaking, the smaller of arc radius is, the lower of the charge transfer resistance will be [18, 19]. As shown in Fig. 4d, the Nyquist plots of all the Fe and S doped g-C$_3$N$_4$ samples demonstrate smaller arc radius attributing to the reduced electronic resistance and increased electronic con-ductivity by doping with Fe and S elements compared to the pure g-C$_3$N$_4$. Similarly, the arc radius for Fe–S codoped g-C$_3$N$_4$ is smallest in all three samples, which is associated with the highest efficiency of the charge separation [25]. Moreover, it is vital that the change trend of the arc radius for g-C$_3$N$_4$ samples is roughly consistent with the results displayed in PL spectra.

The photocatalytic performance of the pure, Fe doped and Fe-S doped g-C$_3$N$_4$ was evaluated by RhB degradation under visible light irradiation ($\lambda > 420$ nm), as shown in Fig. 5a. Before irradiation, the solution is kept in dark room for 30 min. The Fe doped and Fe–S codoped g-C$_3$N$_4$ have slight adsorption effect for RhB compared with the pure one. After 50 min irradiation with visible light, about 51.3% of RhB is degraded in presence of the Fe doped g-C$_3$N$_4$, compared to that of only 33.3% of RhB is decomposed in the pres-ence of the pure g-C$_3$N$_4$. As for the Fe–S codoped g-C$_3$N$_4$, approximately 95% of RhB is decomposed after 50 min vis-ible light irradiation. There is almost no self-degradation of RhB under visible light irradiation in our experiments. RhB is a hazardous pollutant with high extinction coefficient [27]. For the pure and Fe doped g-C$_3$N$_4$, the degradation curve follows a linear equation, $F(x) = -Kt + 1$. As for the Fe–S codoped g-C$_3$N$_4$, the degradation rate follows a logarithm equation, $F(x) = -K\ln(1+t) + 1$.

The results indicated that the codoped g-C$_3$N$_4$ has the highest photocatalytic performance. The excellent photo-catalytic performance of the Fe–S codoped g-C$_3$N$_4$ could be attributed to the following features: the Fe ion imbedded in the avoid triangle increases the active sites for enhanced photocatalytic activity, and exhibits the recombination of photoinduced electron/hole; S atom substituted the edge N of triazine further exhibits the recombination of electron/hole by changing the electronic structure. Figure 5b showed

Fig. 4 **a** UV–Vis absorbance spectra, **b** corresponding Kubelka–Munk plots, **c** PL and **d** EIS spectra of the pure g-C₃N₄ nanosheets (CN) and Fe doped g-C₃N₄ (Fe–CN) and Fe–S codoped g-C₃N₄ (Fe–SN)
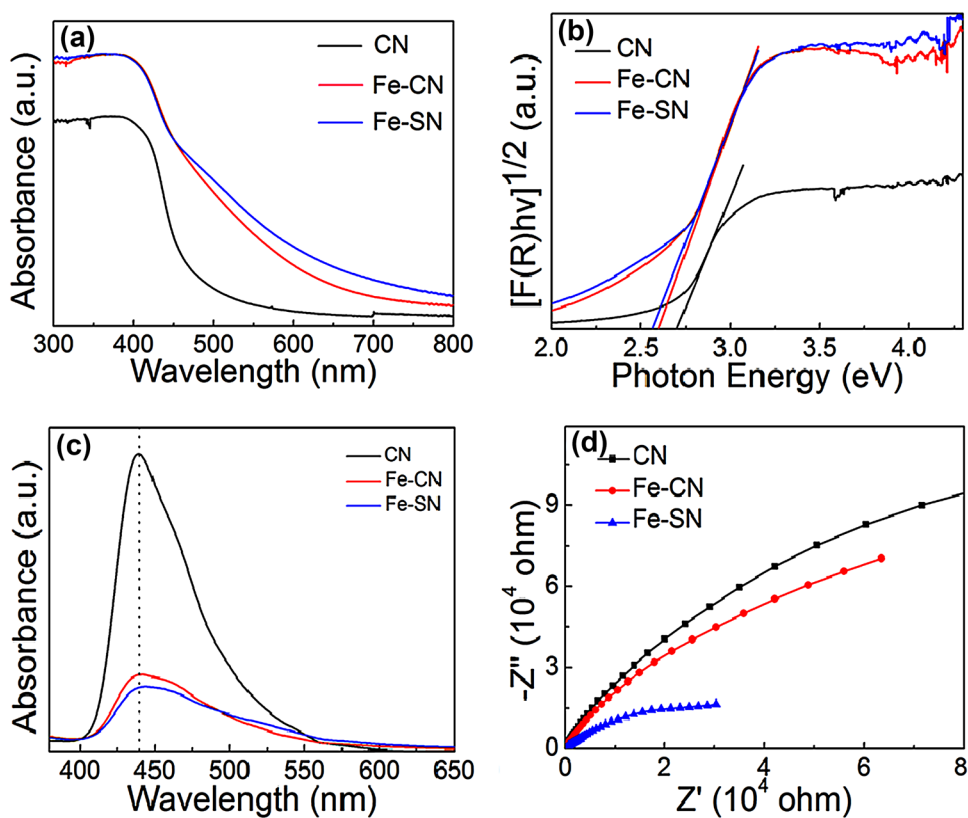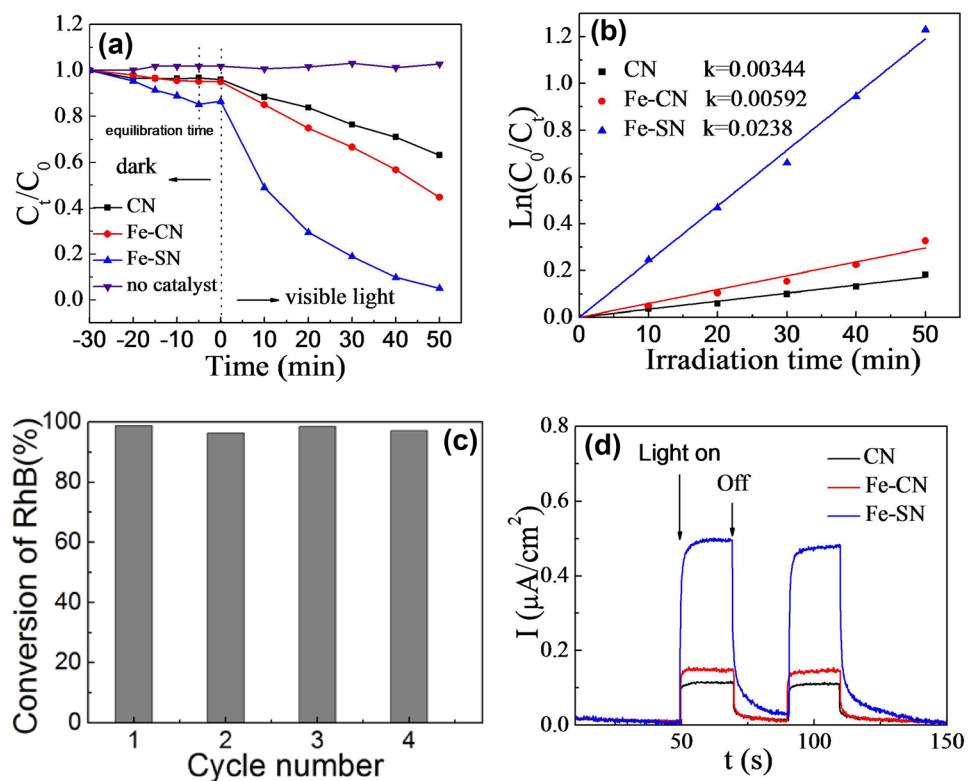

Fig. 5 **a** Photocatalytic performances and **b** corresponding first-order reaction kinetics in the degradation of RhB under visible light irradiation for the pure g-C₃N₄, the Fe doped and Fe–S codoped g-C₃N₄. **c** Stability test of the Fe–S codoped g-C₃N₄. **d** Photocurrent response of the pure, Fe, and Fe + S doped g-C₃N₄

the first-order reaction kinetics for the RhB degradation, which is expressed as

$$-\ln\left(\frac{C_t}{C_0}\right) = kt$$

where k is the reaction rate, and t is the reaction time. The photocatalytic performance of the Fe and Fe–S doped g-C_3N_4 is as 1.8 and 7 times, respectively, as that of the pure g-C_3N_4 calculated from the results in Fig. 5b. The reaction rates are 0.00344, 0.00592, 0.0238 min^{-1} for the pure, Fe doped and Fe–S codoped g-C_3N_4, respectively. The stability of the Fe–S codoped g-C_3N_4 was evaluated by recycle experiments of the RhB degradation. After 3 h visible light irradiation, the catalysts were retrieved by centrifugal and subsequent drying process and used for the next RhB degradation test. The photocatalytic performance was investigated in fresh and three recycles, showed in Fig. 5c. No obvious difference was observed after three recycles, indicating the Fe–S codoped g-C_3N_4 is relatively stable under the visible light irradiation.

The transient photocurrent response of all samples was recorded in Fig. 5d, in which the photocurrent fast increases to a higher value as soon as the irradiation is turn on, and the photocurrent returns to the initial value while the light is turned off. That showed a rapid and steady photocurrent response with reproducibility for each on–off cycle. The current density for Fe–S codoped g-C_3N_4 is about five times that of pure one, revealing the most effective separation and transition of photoinduced electron/hole pairs, which is consistent with PL spectra.

Further theoretical investigation was carried out to study the geometric structure of g-C_3N_4 to confirm Fe coordinated in the pore centre among three heptazine units and the effect of iron and sulfur atomic doping on the electrical structure and catalysis of g-C_3N_4 layer. DFT calculations using the Gaussian09 software package were performed to model the Fe and S doped monolayer g-C_3N_4 with hexagonal honeycomb lattice structure containing three tri-s-triazine units. DFT B3LYP/6-31G(d) level of theory was used to optimize the geometry of g-C_3N_4. DFT B3PW91 was used to calculate the calculation of HOMO and LUMO, the natural orbital population distribution, and DOS based on Fe/Lanl2dz, C N S/6-311(d) level. The pore is the most favorable doping site for Fe atom doped in g-C_3N_4 layer, and the minimum energy structure for S doping is selected as the initiating structure for the following simulation.

The highest occupied molecular orbital (HOMO) and the lowest unoccupied molecular orbital (LUMO) for (001) lattice plane of g-C_3N_4 monolayer were shown in Fig. 6. The calculated HOMO for the pure g-C_3N_4 suggests that the edge N atoms provide the oxidation sites for water to O_2, whereas LUMO indicates the edge C and the inner N atoms are the preferred reduction sites to form H_2 [19]. Figure 6a showed the separation of HOMO and LUMO is quiet small, thus the photoinduced electron/hole can recombine easily, consequently the photocatalysis is quite weak. The migration of the photogenerated e$^-$/h$^+$ pairs is not efficient due to the different localized HOMO and LUMO. No HOMO and LUMO presents on the bridge N atoms inhibiting the carrier migration from one heptazine unit to another and reduces the photcatalytic performance. Figure 6b showed

Fig. 6 Calculated HOMO (top) and LUMO (bottom) of the pure (**a**), S doped (**b**) and **c** Fe doped g-C_3N_4 monolayer. Isosurface is taken at a value of 0.003 e/Bohr^3, Carbon atoms are in grey and nitrogen blue
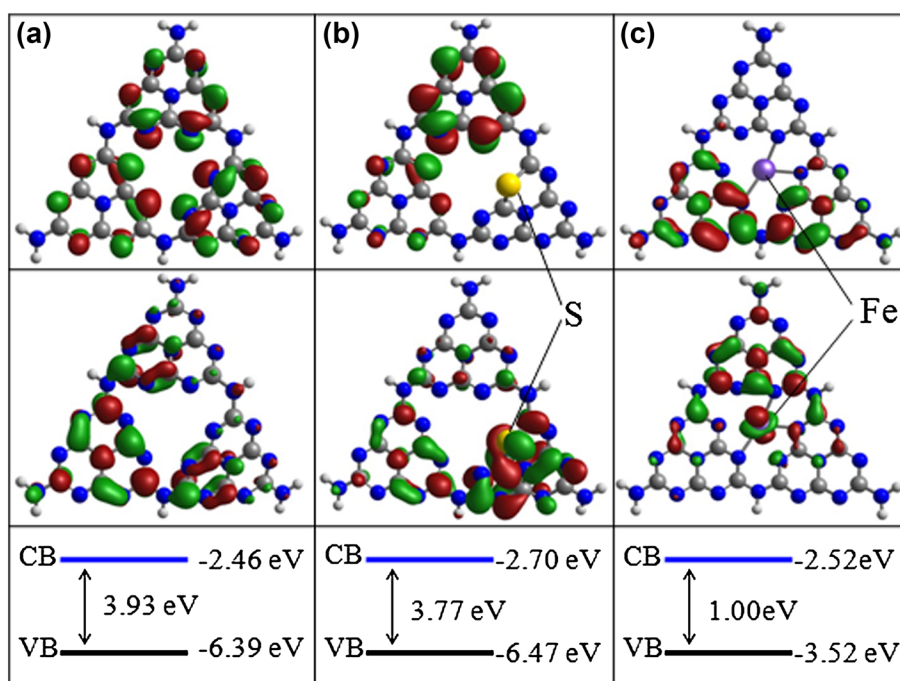
the calculated molecular orbits of S doped g-C_3N_4, which demonstrate the separation of HOMO and LUMO increases distinctly with the sulfur atom doping. The S atoms act as the reduction sites. The substitution of the edge N with S causes slightly stronger delocalized HOMO and LUMO compared to the pure g-C_3N_4 monolayer. The dispersion of the HOMO and LUMO distribution can enhance the carrier mobility. The substitution of the edge N with S causes more stronger delocalized HOMO and LUMO, thus increases the reactive sites [18, 19]. It is noted that the bridge N can act as the channel to connect the adjacent heptazine unit and facilitate the migration of photogenerated electron/hole pairs. The geometry for the S doped g-C_3N_4 monolayer is inclined to deform and become crimped, which is consistent to the morphology shown in the SEM image. Figure 6c showed the calculated molecular orbits of the Fe doped g-C_3N_4. The separation of HOMO and LUMO increases after Fe ion is imbedded in the pore centre among the three triazine units in the layered molecules. The Fe ion exhibits strong reduction property. The corresponding bandgap was illustrated in the bottom part of Fig. 6, which shows the calculated bandgap for the pure, S- and Fe-doped g-C_3N_4 are 3.93, 3.77, and 1.00 eV, respectively. The bandgap decreases with the S and Fe doping, which facilitates the enhancing generation of photoinduced electron/hole pair; the separation of HOMO and LUMO exhibits its recombination. The photcatalytic perfomance thus enhances.

The total and partial DOS for the pure g-C_3N_4 was shown in Fig. 7a. The DOS in valence bond is mainly contributed by the carbon and nitrogen atoms, while the DOS in conductance bond is from the nitrogen atoms. The bandgap is narrowing upon the S and Fe doping and the Fermi level is shifted to the conducting band, as shown in Fig. 7b, c. The intensity and wave profile of the partial DOS for C and N are similar in the ranges of −15 to −5 eV for the g-C_3N_4 monolayer, which indicates the orbitals of C and N hybridized as sp^2. The partial DOS of the bridge N connecting the triazine unit contributes less to total DOS compared with the N atoms in triazine, thus obstructs the transfer of the photoinduced electron/hole pair. The partial DOS of doped S mainly contributes to conduction band, and doped Fe makes even more contribution to conduction band. Therefore, Fe exhibits greater reduction.

The calculated natural orbital population distribution showed that the valence electron configuration of carbon atom is $2s^{0.72-0.74}2p^{2.61-2.62}$, and nitrogen $2s^{1.22-1.37}2p^{4.17-4.42}$. The valence electron of carbon atoms alters to the configuration of $2s^{0.842}p^{2.8}$ and $1s^{0.85}2p^{2.9}$ after the S doping, which demonstrates the S and C bonded with stronger covalent bond, and the modification disappeared far away from the dopant atoms. The valence electron configurations of the doped Fe and S are $3s^{1.66}3p^{4.02}$ and $4s^{0.28}3d^{6.57}4p^{0.22}$, respectively. The electron orbitals of the doped Fe and S have hybridized with that of other atoms, covalently binding with adjacent atoms. The valence electron divergence between the dopant atoms and the adjacent intrinsic atoms yields new energy band in the g-C_3N_4 monolayer, thus changes its photocatalytic performance.

Finally, a tentative mechanism for photocatalytic degradation of RhB was proposed by taking above-mentioned experimental and theoretical strands into consideration. The photocatalytic mechanism of the degradation of RhB was illustrated in Scheme 1. The photoexcited electrons generated from g-C_3N_4 under visible-light irradiation would jump into the conduction band and combine with the dissolved O_2 to form $\cdot O_2^-$, and the Fe^{3+} has lower reduction potential, enhancing the reaction of photoinduced electron and O_2. RhB would be decomposed for the hole in valence band shows intensive photooxidation ability. The photoinduced electron can transfer more easily to Fe(III) and form Fe(II) via the interfacial charge transfer, facilitating the rapid separation of photoinduced electron/hole pair. Thus enhance the mobility of the photoinduced charge and improve the photocatalytic performance. Fe(II) easily tranform into

Fig. 7 Calculated total and partial DOS plots of C, N, Fe and S elements for the pure (**a**), S doped (**b**) and **c** Fe doped g-C_3N_4 monolayer
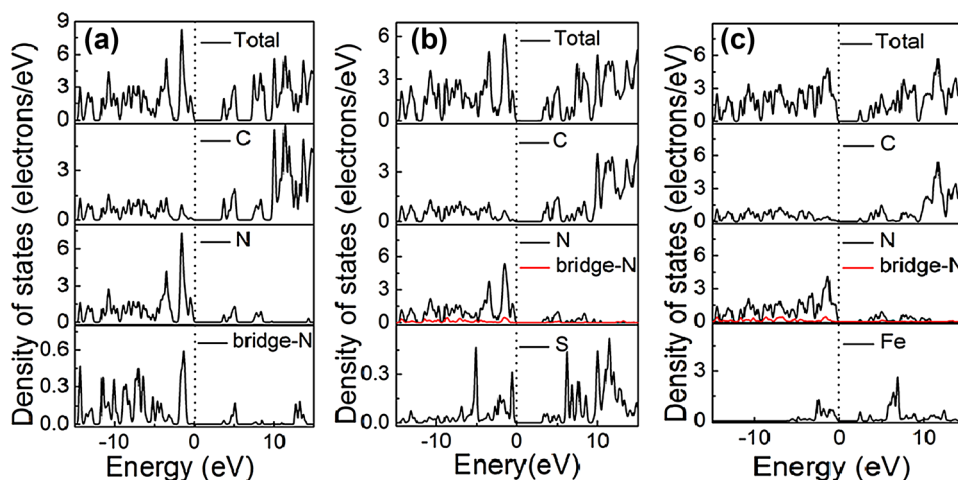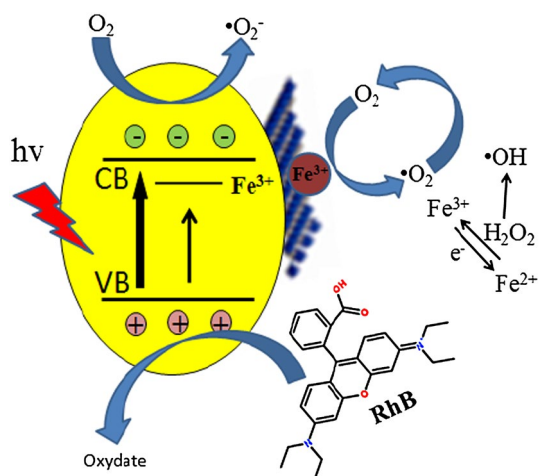
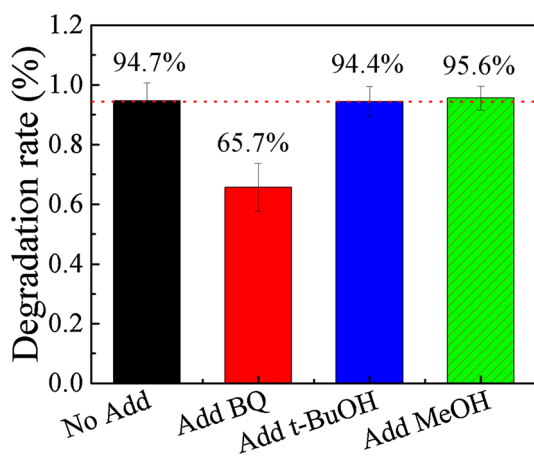**Scheme 1** Photocatalytic degradation of RhB

Fig. 8 The degradation rate of RhB affected by adding different scavengers of BQ, *t*-BuOH and MeOH

Fe(III) through the oxygen reduction, and Fe(III) would be recovered and kept the dynamic equilibrium Fe(III)/Fe(II), companying the generation of H_2O_2. The related reaction equations were listed as follows,

$$e^-_{CB} + O_2 = \cdot O_2^-$$

$$Fe(III) + \cdot O_2^- = Fe(II) + O_2$$

$$Fe(II) + \cdot O_2^- + 2H^+ = Fe(III) + H_2O_2$$
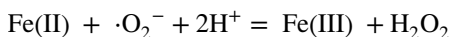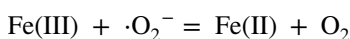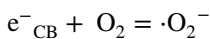
In order to further explain the photocatalytic mechanism of the degradation RhB under visible light, Benzoquinone (BQ, 1.5 mL, 0.1 mM/L), *tert*-butyl alcohol (*t*-BuOH, 1.5 ml) and Methanol (MeOH, 1.5 mL) were added in our model photocatalysis experiments to trap radical superoxide ($\cdot O_2^-$), hydroxyl radicals ($\cdot$OH) and hole (h^+), respectively. The degradation rate did not change obviously by adding

t-BuOH and MeOH in the photocatalytic process, as shown in Fig. 8, indicating hydroxyl radicals and holes are not the reactant for degradating RhB. While the degradation rate decreased dramatically for adding a small amount of BQ, which demonstrated that radical superoxide is the primary reactant in the RhB degradation process. The redox potentials for OH/OH^- and $O_2/\cdot O_2^-$ were determined to be $+1.99$ and -0.33 V, respectively. Theoretically, the conduction band and valence band of g-C_3N_4 were -1.22 and $+1.57$ V [28, 29]. The conduction band of g-C_3N_4 is more negative than the redox potential of $O_2/\cdot O_2^-$, thus O_2 can be reduced to O_2^-. The valence band of g-C_3N_4 is less positive enough to oxide OH^- to $\cdot$OH. That suggested that O_2^- took part in the photocatalytic process, consistent with our experiment.

4 Conclusion

In summary, the Fe and S codoped g-C_3N_4 was successfully prepared by a thermally condensation process of melamine, iron chloride and TCA. Compared to the pure g-C_3N_4 nanosheets, the photocatalytic performance for RhB degradation increased seven times for the Fe–S codoped g-C_3N_4, in which Fe coordinated in the pore centre by forming Fe–N bonds and S atoms substitute the N atoms in the triazine unit. The stronger delocalized HOMO and LUMO and narrower bandgap by Fe and S codoping facilitated the photoexcitation and migration of photoinduced charge carriers, thus enhanced the photocatalytic performance. The experimental and theoretical results showed that the band structure of g-C_3N_4 could be tuned via Fe + S doping, thus improved the photocatalytic performance. This study may provide a pathway to engineering the band structure of photocatalysts by using metal and nonmetal codoping method.

Author Contributions The manuscript was written through contributions of all authors. All authors have given approval to the final version of the manuscript.

References

1. Wang X, Maeda K, Thomas A, Takanabe K, Xin G, Carlsson JM, Domen K, Antonietti M (2009) A metal-free polymeric photocatalyst for hydrogen production from water under visible light. Nat Mater 8:76–80
2. Ong WJ, Tan LL, Ng YH, Yong ST, Chai SP (2016) Graphitic carbon nitride (g-C_3N_4)-based photocatalysts for artificial photosynthesis and environmental remediation: are we a step closer to achieving sustainability? Chem Rev 116:7159–7329
3. Jorge AB, Martin DJ, Dhanoa MTS, Rahman AS, Makwana N, Tang J, Sella A, Cora F, Firth S, Darr JA, McMillan PF (2013) H_2

and O_2 evolution from water half-splitting reactions by graphitic carbon nitride materials. J Phys Chem C 117:7178–7185

4. Yan H (2012) Soft-templating synthesis of mesoporous graphitic carbon nitride with enhanced photocatalytic H_2 evolution under visible light. Chem Commun 48:3430–3432

5. Zhang J, Guo F, Wang X (2013) An optimized and general synthetic strategy for fabrication of polymeric carbon nitride nano-architectures. Adv Funct Mater 23:3008–3014

6. Li P, Zhang W, Zhang Y, Sun Y, Dong F (2016) $(NH_4)_2SO_4$-assisted polycondensation of dicyandiamide for porous g-C_3N_4 with enhanced photocatalytic NO removal. RSC Adv 6:96334–96338

7. Kumar S, Surendar T, Baruah A, Shanker V (2013) Synthesis of a novel and stable g-C_3N_4–Ag_3PO_4 hybrid nanocomposite photocatalyst and study of the photocatalytic activity under visible light irradiation. J Mater Chem A 1:5333–5340

8. Kumar S, Baruah A, Tonda S, Kumar B, Shanker V, Sreedhar B (2014) Cost-effective and eco-friendly synthesis of novel and stable N-doped ZnO/g-C_3N_4 core-shell nanoplates with excellent visible-light responsive photocatalysis. Nanoscale 6:4830–4842

9. Zhang J, Zhang G, Chen X, Lin S, Möhlmann L, Dołęga G, Lipner G, Antonietti M, Blechert S, Wang X (2012) Co-monomer control of carbon nitride semiconductors to optimize hydrogen evolution with visible light. Angew Chem Int Ed 124:3237–3241

10. Chen L, Man YH, Chen ZQ, Zhang YP (2016) Ag/g-C_3N_4 layered composites with enhanced visible light photocatalytic performance. Mater Res Express 3:115003

11. Ge L, Han C, Liu J, Li Y (2011) Enhanced visible light photocatalytic activity of novel polymeric g-C_3N_4 loaded with Ag nanoparticles. Appl Catal A 409:215–222

12. Yu J, Wang K, Xiao W, Cheng B (2014) Photocatalytic reduction of CO_2 into hydrocarbon solar fuels over g-C_3N_4–Pt nanocomposite photocatalysts. Phys Chem Chem Phys 16:11492–11501

13. Ni Z, Dong F, Huang H, Zhang Y (2016) New insights into how Pd nanoparticles influenced the photocatalytic oxidation and reduction ability of g-C_3N_4 nanosheets. Catal Sci Technol 6:6448–6458

14. Yan SC, Li ZS, Zou ZG (2010) Photodegradation of rhodamine B and methyl orange over boron-doped g-C_3N_4 under visible light irradiation. Langmuir 26:3894–3901

15. Gao D, Liu Y, Liu P, Si M, Xue D (2016) Atomically thin B doped g-C_3N_4 nanosheets: high-temperature ferromagnetism and calculated half-metallicity. Sci Rep 6:35768

16. Sagara N, Kamimura S, Tsubota T, Ohno T (2016) Photoelectrochemical CO_2 reduction by a p-type boron-doped g-C_3N_4 electrode under visible light. Appl Catal B 192:193–198

17. Zhang Y, Mori T, Ye J, Antonietti M (2010) Phosphorus-doped carbon nitride solid: enhanced electrical conductivity and photocurrent generation. J Am Chem Soc 132:6294–6295

18. You R, Dou H, Chen L, Zheng S, Zhang Y (2017) Graphitic carbon nitride with S and O codoping for enhanced visible light photocatalytic performance. RSC Adv 7:15842–15850

19. Li J, Shen B, Hong Z, Lin B, Gao B, Chen Y (2012) A facile approach to synthesize novel oxygen-doped g-C_3N_4 with superior visible-light photoreactivity. Chem Commun 48:12017–12019

20. Ma H, Li Y, Li S, Liu N (2015) Novel P–O codoped g-C_3N_4 with large specific surface area: hydrothermal synthesis assisted dissolution-precipitation process and their visible light activity under anoxic conditions. Appl Surf Sci 357:131–138

21. Cui J, Liang S, Wang X, Zhang J (2015) First principle modeling of oxygen-doped monolayer graphitic carbon nitride. Mater Phys Chem 161:194–200

22. Liu Q, Guo Y, Chen Z, Zhang Z, Fang X (2016) Constructing a novel ternary Fe(III)/graphene/g-C_3N_4 composite photocatalyst with enhanced visible-light driven photocatalytic activity via interfacial charge transfer effect. Appl Catal B 183:231–241

23. Zhang S, Li J, Zeng M, Li J, Xu J, Wang X (2014) Band engineering and mechanism study of nonmetal and metal ion codoped carbon nitride: C + Fe as an example. Chem Eur J 20:9805–9812

24. Tian J, Liu Q, Asiri AM, Qusti AH, Al-Youbi AO, Sun X (2013) Ultrathin graphitic carbon notride nanosheets: a novel peroxidase mimetic, Fe doping-mediated catalytic performance enhancement and application to rapid highly sensitive optical detection of glucose. Nanoscale 5:11604–11609

25. Oh Y, Hwang JO, Lee E, Yoon M, Le VD, Kim YH, Kim DH, Kim SO (2016) Divalent Fe atom coordination in two-dimensional microporous graphitic carbon nitride. ACS Appl Mater Interface 8:25438–25443

26. Le S, Jiang T, Zhao Q, Liu X, Li Y, Fang B, Gong M (2016) Cu-doped mesoporous graphitic carbon nitride for enhanced visible-light driven photocatalysis. RSC Adv 6:38811–38819

27. Bahreman A, Cuello-Garibo J, Bonnet S (2014) Yellow-light sensitization of a ligand photosubstitution reaction in a ruthennium polypyridyl complex covalently bound to a rhodamine dye. Dalton Trans 43:4494–4505

28. Chen X, Zhang J, Fu X, Antonietti M, Wang X (2009) Fe-g-C_3N_4-catalyzed oxidation of benzene to phenol using hydrogen peroxide and visible light. J Am Chem Soc 131:11658–11659

29. Mrowetz M, Balcerski W, Colussi AJ, Hoffmann MR (2004) Oxidative power of nitrogen-doped TiO_2 photocatalysts under visible illumination. J Phys Chem B 108:17269–17273